coatings

MDPI

Article

Multi-Objective Optimization of Process Parameters in Laser DED Ni-Based Powder on Steel Rail Using Response Surface Design

Juncai Li [1,2,3], Yue Yang [1,2], Liaoyuan Chen [1,2], Tianbiao Yu [1,2,*], Ji Zhao [1,2,*] and Zixuan Wang [1,2]

1 School of Mechanical Engineering and Automation, Northeastern University, Shenyang 110819, China
2 Liaoning Provincial Key Laboratory of High-End Equipment Intelligent Design and Manufacturing Technology, Shenyang 110819, China
3 Key Laboratory of Data Analytics and Optimization for Smart Industry (Northeastern University), Ministry of Education, Shenyang 110819, China
* Correspondence: tianbiaoyudyx@gmail.com (T.Y.); jzhao@mail.neu.edu.cn (J.Z.)

Abstract: With the rise of global industrialization, the requirements for the operating speed and carrying capacity of high-speed trains are increasingly higher. Because the wear and tear of rails gradually increases during the running of high-speed trains, strengthening or repairing rail surfaces is of paramount significance. Laser-directed energy deposition (DED) exhibits significant advantages in improving surface hardness, corrosion resistance, and abrasion resistance. Because of the multiple interacting optimization objectives, the development of a multi-objective optimization method for process parameters is significant for improving DED deposition quality. Response surface design employs multivariate quadratic regression equations to fit the functional relationship between the factors and the responses, which can be employed to find the optimal process parameters and solve multivariate problems. This study develops a multi-objective optimization model with response surface design and 2D process mappings to visually analyze the effects of scanning speed, laser power, and powder feed rate on aspect ratio, dilution rate, and microhardness. The optimal combination of process parameters for Ni-based alloys on U71Mn rail is a laser power of 431 W, a scanning speed of 5.34 mm/s, and a powder feed rate of 1.03 r/min. In addition, a multi-physics field finite element model is developed to analyze the evolution mechanism of the microstructure from the bottom to the top of the single track. This study can provide theoretical and technical support for the surface strengthening or repair of U71Mn rail.

Keywords: laser-directed energy deposition; U71Mn rail; multi-objective optimization; response surface design; geometrical characteristics; microstructure evolution

check for updates

Citation: Li, J.; Yang, Y.; Chen, L.; Yu, T.; Zhao, J.; Wang, Z. Multi-Objective Optimization of Process Parameters in Laser DED Ni-Based Powder on Steel Rail Using Response Surface Design. *Coatings* **2024**, *14*, 401. https://doi.org/10.3390/coatings14040401

Academic Editors: Rafael Comesaña, Emmanuel P. Georgiou and Angelos Koutsomichalis

Received: 18 February 2024
Revised: 16 March 2024
Accepted: 18 March 2024
Published: 28 March 2024

1. Introduction

The rail transition is an economic artery closely related to daily life and pivotal in the economy and society [1,2]. Rails are one of the critical components of the wheel and rail transportation system and the basis for train operations. With the development of rail transportation technology, the maximum running speed of high-speed trains has been gradually increased from 100 to 300 km/h. The rail loading environment is becoming more complex and demanding, resulting in harsher working conditions for the wheel–rail friction pair. The rail surface is susceptible to wear, corrosion, and failure under the conditions of side grinding and crushing, which decreases the smoothness and safety of train operation [3]. Therefore, it is essential to employ surface-strengthening technology to improve the hardness, wear resistance, and corrosion resistance of rails, thus prolonging their service life. It is of essential practical value and practical significance for reducing the difficulty of railroad maintenance, reducing the cost of railroad maintenance, and guaranteeing the efficiency of train operation [4].

Laser-directed energy deposition (DED) is a new surface repair or modification technology that has emerged over recent years [5,6]. The deposition material and substrate surface material on the rail are rapidly melted by laser energy to form a molten pool. Under the self-cooling effect of the rail substrate, the molten pool solidifies quickly to form a coating metallurgically bonded to the substrate. Therefore, by designing the composition of the deposited powder, the microhardness, wear resistance, and resistance to high temperatures of the rail can be significantly improved [3]. Because the DED process is characterized by complex physicochemical behavior, it is crucial to select a suitable combination of process parameters to obtain a high-quality cladding layer [7,8]. In addition, DED is a complex nonlinear process covering the coupling of multiple process parameters, resulting in significant difficulties in qualitatively characterizing the mapping relationship between individual process parameters and the quality of the cladding layer [9,10].

For the multi-objective optimization of process parameters in the DED process, many scholars have conducted research on orthogonal experimental design, response surface analysis, and gray correlation analysis. Ma et al. [11] first explored the factors affecting the morphology of the cladding layer by the orthogonal experimental method and obtained the combination of process parameters under optimal quality by polar analysis and calculation of gray correlation degree prediction. The results showed that laser power and scanning speed affected the forming quality among the various influencing factors. Ansari et al. [12] presented an empirical statistical model for DED optimization for In718 and analyzed the effects of key process parameters on the geometric characteristics of single tracks. Processing diagrams are practically usable for selecting appropriate processing parameters for specific equipment and materials. Intelligent optimization methods are on-the-fly search algorithms based on artificial intelligence or natural phenomena that allow various behaviors to be abstracted into quantifiable key indicators and transformed into mathematical problems to be solved, mainly including BP neural networks and particle swarm algorithms [13,14]. Based on the experimental data of laser powder deposition of iron-based alloy coatings on ASTM36 substrate, Sohrabpoor [15] developed an adaptive neuro-fuzzy inference model to predict the geometrical characteristics of the deposited layers. The results indicate that an artificial neural network (ANN) can effectively solve the multi-objective optimization problem related to process parameters in the DED process. To obtain the optimal parameters of cobalt-based alloy coatings, Guo et al. [16] trained experimental data using the BP neural network to determine the mapping relationship between process parameters and mechanical performance. Comparing the predicted and experimental results, the average relative error was not more than 10%. This proves the feasibility of the model and demonstrates the optimization of the process parameters. However, this method requires a large amount of experimental data. Ma et al. [11] employed a particle swarm algorithm to optimize the laser power, scanning speed, and defocus amount to fabricate coatings with a low dilution rate and residual stress. However, the intelligent optimization method not only requires a large amount of data to be trained and validated but also suffers from the problems of slow convergence, tedious and cumbersome processes, and a lack of explicit function expression.

Overall, response surface methodology represents certain advantages in dealing with nonlinear problems containing multiple factors and enables more experimental information to be obtained with a limited number of trials [17,18]. It is possible to obtain the relationship between one or more response targets and input responses, thereby obtaining the optimal multivariate parameters more reliably [19]. Therefore, this study selected the commonly used modified rail steel U71Mn steel as the deposition substrate. Due to the high corrosion resistance required of the repaired steel rail and the ability of Ni and Fe atoms to replace each other, the nickel-based self-soluble powder Ni45 was selected as the deposited material. Local repair of damaged guide rails can reduce the consumption of Ni-based alloys and the waste of rare and precious metals. The response surface method was employed to optimize the laser power (P), scanning speed (Vs), and powder feed rate (V_f) of the Ni-based powder

coated on the rail surface to obtain a suitable process combination. This study aims to provide a foundation for the repair or strengthening of high-speed rails.

2. Optimization Process

The central composite test design comprises a zero-level main test point, an axial test point, and a cubic test point [20]. The regression relationship between process parameters and response indicators can be expressed as follows:

$$y_u = \phi(x_{1u}, x_{2u}, \cdots x_{ku}) + \varepsilon_u \tag{1}$$

where μ denotes the number of designed experiments; k denotes the number of process parameters; $x_{k\mu}$ indicates the level of the kth factor at the uth test; and the Φ is the response function.

This study developed a second-order polynomial regression model to fit the experimental data to assess the effect of process parameters and response indexes. The functional relationship can be expressed as follows:

$$y_u = \beta_0 + \beta_1 x_{1u} + \beta_2 x_{2u} + \beta_{11} x_{1u}^2 + \beta_{22} x_{2u}^2 + \beta_{12} x_{1u} x_{2u} + \varepsilon_u \tag{2}$$

where y is the predicted response value; β_0 is the intercept; β_i, β_{ii}, and β_{ij} are the regression coefficients; and ε is the test error.

To evaluate the regression credibility, it is necessary to analyze the variance (ANOVA) of the established regression model by assessing its significance. The detailed process is as follows:

(1) Calculate the sum of squares of the deviations

The factor variable total sum of squares (SS_t), the factor variable residual sum of squares (SS_e), and the factor regression sum of squares (SS_r) can be expressed as follows:

$$\begin{cases} SS_t = \sum\limits_{i=1}^{n} (y_i - \overline{y})^2 = SS_e + SS_r \\ SS_e = \sum\limits_{i=1}^{n} (y_i - \hat{y}_i)^2 \\ SS_r = \sum\limits_{i=1}^{n} (\hat{y}_i - \overline{y})^2 \end{cases} \tag{3}$$

where y_i is the experimental value of the response, $\overline{y}$ is the mean value of the reaction, and $\hat{y}_i$ is the regression estimate of the response.

(2) Calculate freedom degrees

The degrees of freedom corresponding to each type of sum of squares are df_t, df_e, df_r, and their expressions are as follows:

$$\begin{cases} df_t = n - 1 \\ df_r = 2p + p(p-1)/2 \\ df_e = f_t - f_r \end{cases} \tag{4}$$

where n denotes the sum of the degrees of freedom.

(3) Calculate average mean square

The average mean squared error (MS) indicates the ratio of each sum of squares to its degrees of freedom, and R^2 is employed to indicate the correlation of the regression model. If the value of R^2 is closer, it means that the regression model correlation is better, and its expression is as follows:

$$MS = \frac{SS_t}{df_e} \tag{5}$$

(4) Calculate *F*- and *p*-values

The *F*-value, also known as the *F*-test statistic, is designed to characterize the goodness of fit of a regression model. A larger *F*-value indicates a better fit and better significance. The *F*-value expression is as follows:

$$F = \frac{SS_r/df_r}{SS_e/df_e} \sim F(df_r, df_e) \tag{6}$$

The *p*-value indicates the probability that the difference between the factors resulted from sample error, which can be applied to determine the significance of the model, taking the significance level of 0.05. When *p* is greater than 0.05, the regression model is not significant. When *p* is less than 0.05, the model is effective. Moreover, smaller *p*-values indicate that the process parameter exerts a more significant effect on the corresponding target.

The aspect ratio and dilution rate are the two leading indicators that affect the deposition and bonding strength of the solidified coating. When the aspect ratio is less than 2, the clad height is large, and the melt pool edge is prone to collapse. On the contrary, when the aspect ratio exceeds 2, the clad lies flat on the substrate, with fewer defects in the lapping zone and high deposition quality. In addition, microhardness is an essential indicator for evaluating the mechanical properties of the coating. The dilution rate is employed to characterize the extent to which the melting of the substrate results in a variation in the composition of the clad. Too large a dilution rate weakens the performance of the single track. However, too low a dilution rate can lead to poor metallurgical bonding between the clad and the substrate, resulting in peeling from the substrate. In this study, based on the multi-objective optimization theory, the maximum aspect ratio, maximum microhardness, and minimum dilution rate were expected. The process parameter level ranges were set as constraints to achieve a multi-objective optimization study of DED process parameters with the aid of the Design Expert software v11.0. The detailed flow of the optimization process is shown in Figure 1.

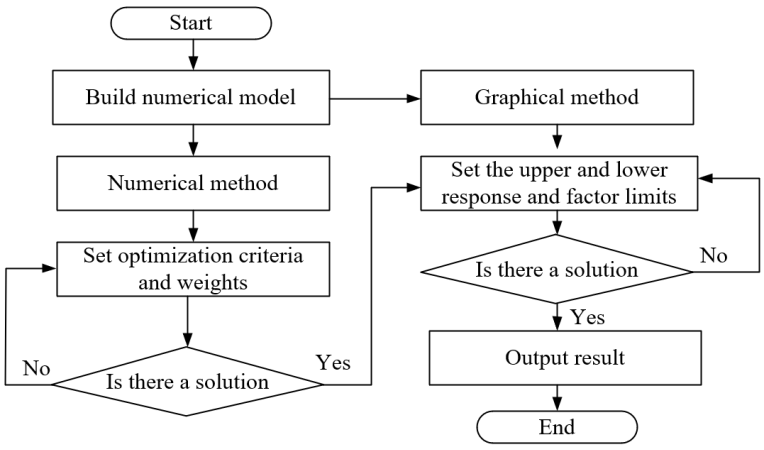

Figure 1. Multi-objective optimization flow of process parameters based on response surface design.

3. Experimental

Standard high-specification U71Mn rails are shown in Figure 2a. A substrate of $100 \times 70 \times 10$ mm^3 was machined by wire EDM technology, and the ground substrate is shown in Figure 2b. Ni45 self-fusing alloy was chosen as the deposited material because of its effective resistance to corrosion, abrasion, and impermissibility with rail steel. The scanning electron microscopy (SEM) images of Ni45 self-fluxing powder are shown in Figure 2c. The chemical compositions of U71Mn rail and Ni45 powder are shown in Table 1.

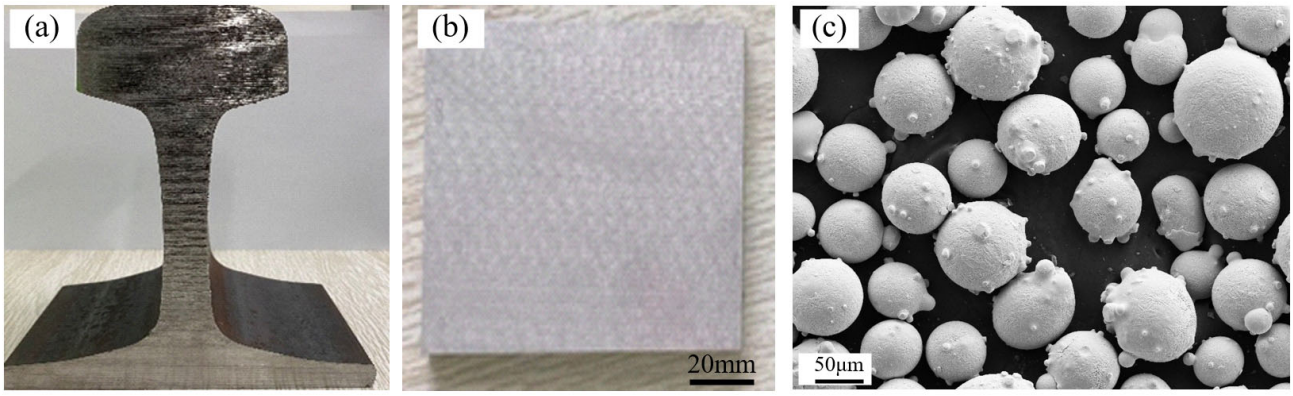

Figure 2. Experimental material: (**a**) U71Mn rail, (**b**) ground substrate, and (**c**) Ni45 powder.

Table 1. Chemical composition of Ni45 powder and U71Mn steel.

Element	C	Cr	Si	Fe	B	Mn	P	S	Ni
Ni-based powder	0.45	12.00	4.0	10.00	2.40	0.10	-	-	Bal.
U71Mn steel	0.65–0.76	-	0.15–0.35	Bal.	-	1.10–1.40	≤0.030	≤0.030	-

Based on the pre-completed one-factor experiments, the process parameters were optimized for the single tracks, and the levels of the process parameters are shown in Table 2. Based on a central composite design with a factor of 2 and a level of 5, 20 group experiments were designed, as shown in Table 3.

Table 2. The level of process parameters for the response surface.

Parameters	Unit	Levels				
		−1.68	−1	0	+1	+1.68
Laser Power (P)	(W)	409.77	420	435	450	460.23
Sanning speed (Vs)	(mm/s)	3.32	4	5	6	6.68
Power feed rate (V_f)	(r/min)	0.83	0.9	1	1.10	1.17

Table 3. Central composite trial design and measured results.

Std	Run	Laser Power P (W)	Scanning Speed V_s (mm/s)	Power Feed Rate V_f (r/min)	Aspect Ratio ζ	Dilution Ratio η	Microhardness ($HV_{0.3}$)
#1	11	420.00	4.00	0.90	2.26	0.3354	428.55
#2	9	450.00	4.00	0.90	2.34	0.3427	417.13
#3	13	420.00	6.00	0.90	2.18	0.3512	455.53
#4	6	450.00	6.00	0.90	2.77	0.4174	435.4
#5	19	420.00	4.00	1.10	2.25	0.2845	438.92
#6	8	450.00	4.00	1.10	2.12	0.3351	420.23
#7	10	420.00	6.00	1.10	2.34	0.3256	462.11
#8	3	450.00	6.00	1.10	2.71	0.3871	450.19
#9	7	409.77	5.00	1.00	2.01	0.3064	434.19
#10	4	460.23	5.00	1.00	2.34	0.3812	412.81
#11	2	435.00	3.32	1.00	2.42	0.3342	428.08
#12	18	435.00	6.68	1.00	2.98	0.3878	470.26
#13	17	435.00	5.00	0.83	2.24	0.3423	442.79
#14	15	435.00	5.00	1.17	2.25	0.3115	447.82
#15	5	435.00	5.00	1.00	2.98	0.3434	446.82
#16	14	435.00	5.00	1.00	2.99	0.3426	461.49

Table 3. *Cont.*

Std	Run	Laser Power P (W)	Scanning Speed V_s (mm/s)	Power Feed Rate V_f (r/min)	Aspect Ratio ζ	Dilution Ratio η	Microhardness ($HV_{0.3}$)
#17	20	435.00	5.00	1.00	2.94	0.3189	460.78
#18	1	435.00	5.00	1.00	3.04	0.3494	459.63
#19	16	435.00	5.00	1.00	3.22	0.3266	453.31
#20	12	435.00	5.00	1.00	2.74	0.3328	460.8

The experiments were conducted on a laser DED system, as shown in Figure 3a. The DED system consisted of the following key components: a KUKA robot, a cladding head, a controller, a water cooler, a powder feeder, and an electrical control cabinet. The laser generator provided enough energy to melt the substrate and the deposited material to form a molten pool, which rapidly solidified to form the clad, as shown in Figure 3b. The process mainly consisted of the following steps: drying the powder, writing the program, conducting the experiments, and characterizing the results.

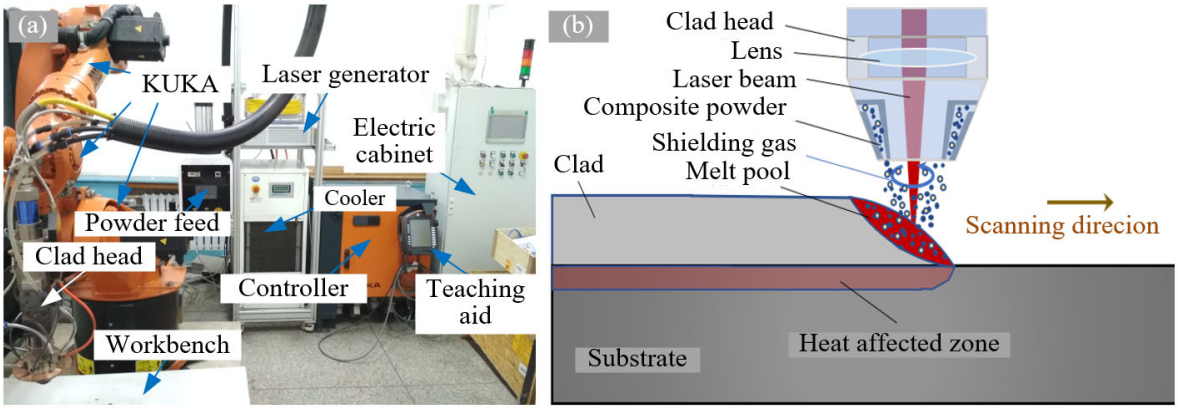

Figure 3. Experimental equipment: (**a**) actual and (**b**) schematic.

After the experiment, the cross section of single tracks was obtained by cutting the substrate perpendicular to the scanning direction using EDM technology. The cross section was ground alternately by sandpaper of 240 to 2000 grit, followed by metallurgical polishing to achieve a mirror-like finish. The cross-sectional morphology of the single track was obtained by 3D laser confocal microscopy (Japan) as well as the measurement of the height, width, and depth of the melt pool by the integrated software, as shown in Figure 4a. The aspect ratio (ξ) and dilution rate (D) can be calculated as follows:

$$\xi = W/H \tag{7}$$

$$D = \frac{h}{H+h} \tag{8}$$

where W is the clad width, H is the clad height, and h is the pool depth.

The polished specimens were etched by aqua regia for 30 s. The grain characteristics at different locations of the single track were gathered by laser confocal microscopy, as shown in Figure 4a. The Vickers hardness tester (China) was used to obtain the micro-hardness of a single track, and the mean value of three selected points on the fusion cladding was considered the average micro-hardness, as shown in Figure 4b. The optical cross-sectional morphology of the single tracks is shown in Figure 5. It can be noticed that a good metallurgical bond was formed between all single tracks and the substrate. Under the strong Marangoni convection in the molten pool, the high-temperature liquid on the surface of the molten pool flowed towards the bottom of the molten pool, increasing

the dilution rate and bond strength. In addition, as a result of the large surface tension coefficient at the gas–liquid interface of the molten pool, the single-pass track surface at the end of solidification exhibited a rounded shape, which is beneficial for improving the quality of the multi-pass overlap in the laser cladding repair process. The experimental results of the aspect ratio, dilution rate, and microhardness of the single tracks are shown in Table 3.

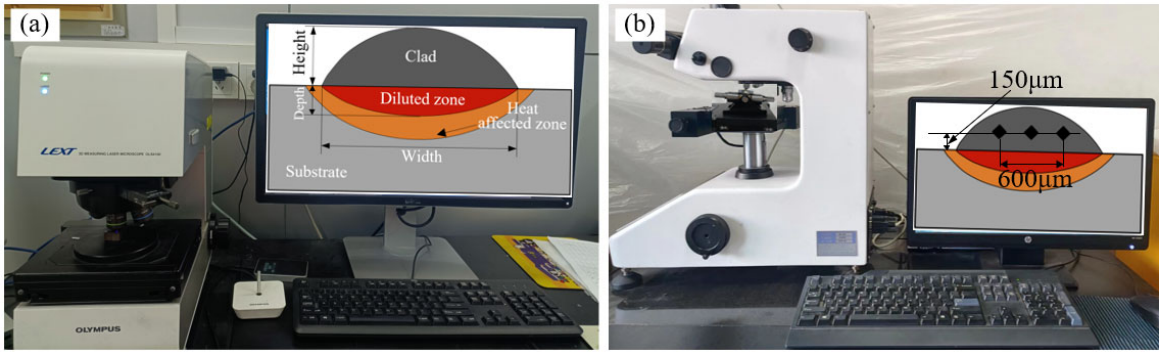

Figure 4. Characterization equipment: (**a**) 3D laser confocal microscopy and (**b**) Vickers hardness tester.

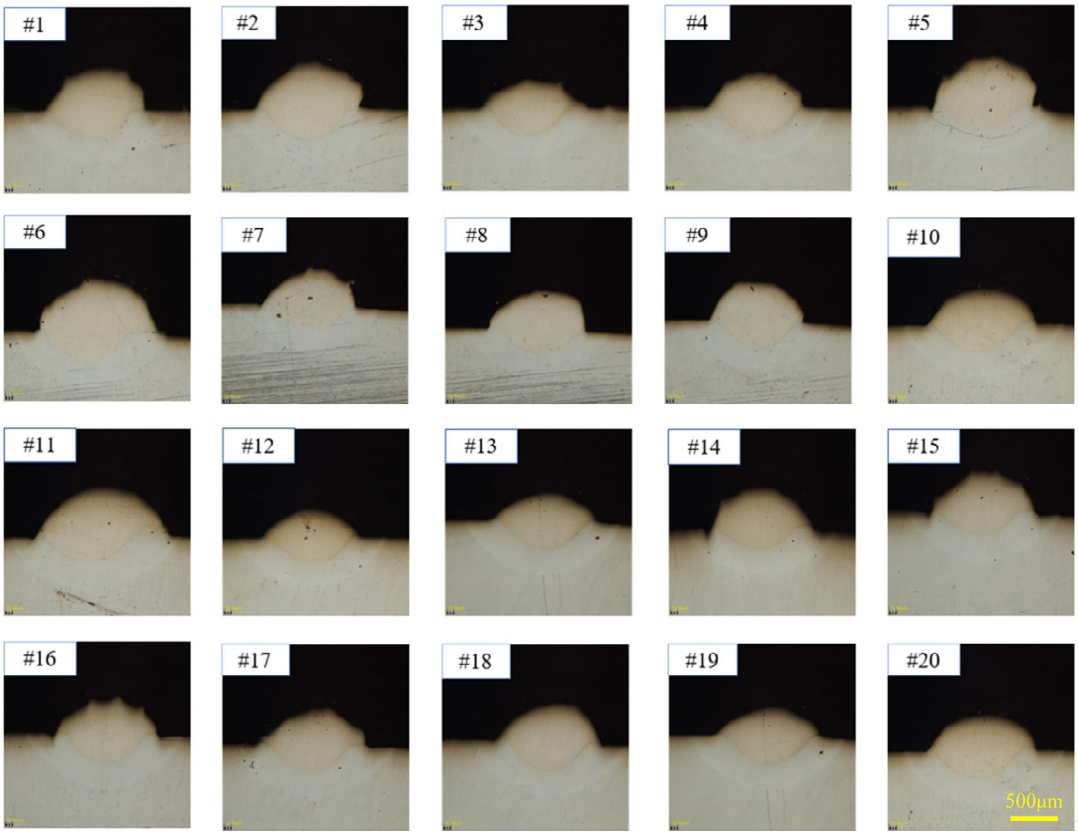

Figure 5. Cross-sectional morphologies of single tracks.

4. Results and Discussion

4.1. Response Surface Analysis for Aspect Ratio

The process parameters and aspect ratios were analyzed by ANOVA, and the results are shown in Table 4. It can be seen that the *F*-value is 22.12 with a *p*-value less than 0.0001, indicating that the established quadratic regression model for aspect ratio is valid and highly significant. Its loss of fit is not significant, proving the fitted equation is reliable. The signal-to-noise ratio of 12.169 is more than 4, indicating high precision and accuracy [21,22].

The R^2 value is 0.8877, indicating a good correlation. Figure 6a presents the residual plot of the aspect ratio model. No abnormal values exist, indicating that the model is credible. Figure 6b shows the measured and predicted values of the aspect ratio. It can be noticed that the experimental values are more centrally distributed on both sides of the fitted straight line, which also indicates the accuracy of the model [23]. In summary, the insignificant factors in the model were removed to develop a quadratic regression model for the effect of process parameters on the aspect ratio. The final regression model for the aspect ratio is as follows:

$$\xi = 2.98 + 0.11A + 0.14B - 0.28A^2 - 0.093B^2 - 0.25C^2 \quad (9)$$

where A, B, and C in Equation (9) can be found in Table 4.

Table 4. ANOVA for the aspect ratio.

	Sum of Square	Freedom Degrees	Mean Squares	*F*-Value	*p*-Value	
Model	2.34	5	0.47	22.12	<0.0001	Significant
A Laser power	0.16	1	0.16	7.43	0.0164	
B Scanning speed	0.28	1	0.28	13.46	0.0025	
A^2	1.12	1	1.12	53.02	<0.0001	
B^2	0.13	1	0.13	5.94	0.0288	
C^2	0.93	1	0.93	44.03	<0.0001	
Residual	0.3	14	0.021			
Anomaly	0.18	9	0.02	0.81	0.6306	Not significant
Pure error	0.12	5	0.024			
Sum of all	2.64	19				
Standard deviation	0.15		R^2	0.8877		
Mean	2.56		Adjusted R^2	0.8475		
Variation coefficient	5.69		Projected R^2	0.8151		
Predicting the residual sum of squares	0.49		Signal-to-noise ratio	12.169		

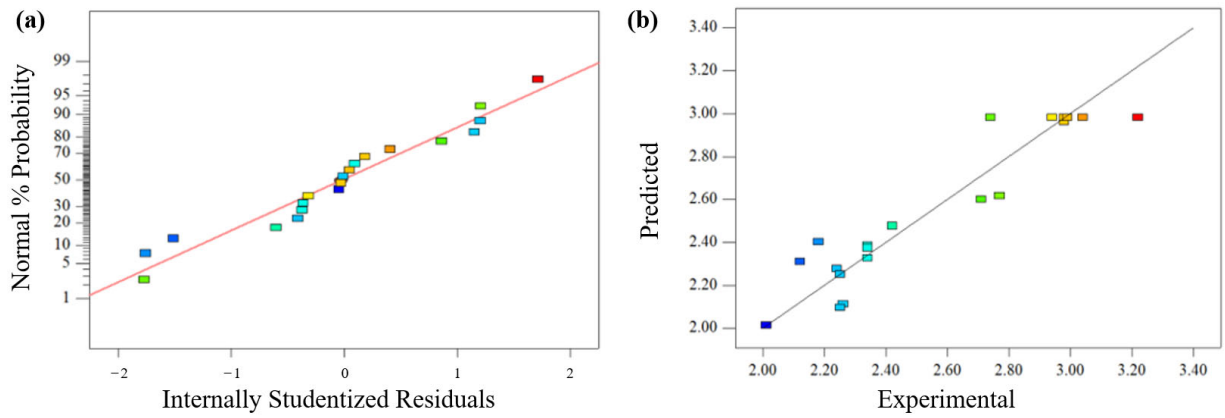

Figure 6. Fitting of process parameters to the aspect ratio: (**a**) residual and (**b**) comparison of measured and predicted values.

The *p*-values regarding laser power and scanning speed are less than 0.05, indicating that both factors significantly affect the aspect ratio. In contrast, the effect of powder feed rate on the aspect ratio is insignificant. Therefore, contour plots and 3D response surface plots of scanning speed and laser power concerning aspect ratio were developed. Figure 7 shows that the aspect ratio increases gradually as the laser power decreases and the scanning speed increases. The decrease in laser power and increase in scanning speed can decrease the laser energy and powder density. As a result, the height and width of the single-pass deposition are significantly reduced. At the same time, the liquid at the center of the melt pool flows toward its edges due to negative surface tension [24,25]. This behavior results in an increase in width and a decrease in height, increasing the aspect ratio.

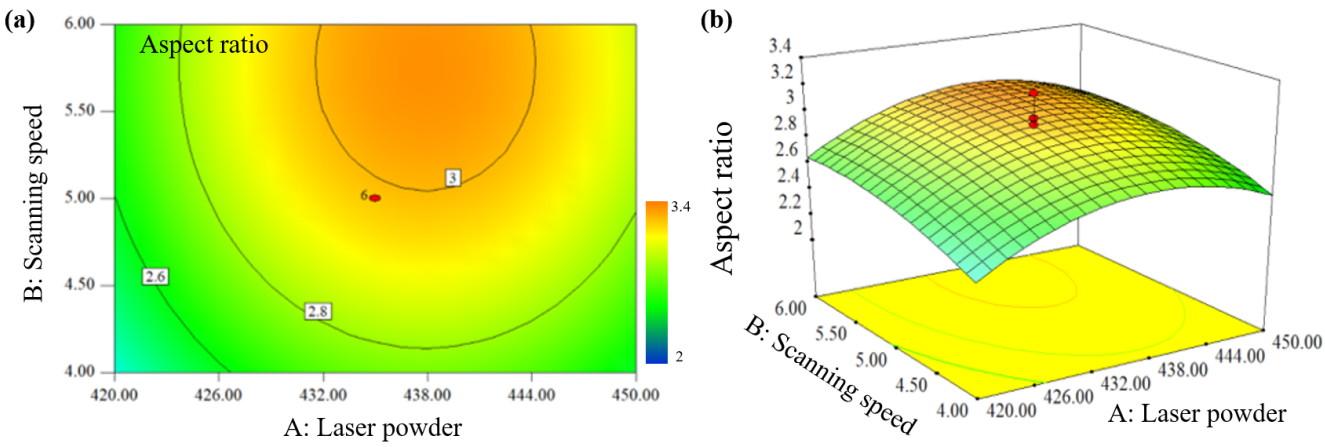

Figure 7. Response of laser power and scanning speed to the aspect ratio: (**a**) contour plot, (**b**) 3D surface.

4.2. Response Surface Analysis for the Dilution Rate

Table 5 lists the ANOVA results of the process parameters on the dilution rate. It can be seen that the *F*-value is 25.68 with a *p*-value of less than 0.0001, indicating that the established quadratic regression model for dilution rate is valid and highly significant. Its fit loss is insignificant, proving that the fitted equation is reliable. The signal-to-noise ratio of 17.668 is more than 4, indicating a high degree of accuracy and precision. The R^2 value of 0.8726 indicates a strong correlation [17]. The residual plot for the dilution rate model is shown in Figure 8a. The absence of abnormal values indicates a high confidence level in the model. Figure 8b compares the measured and predicted values of the dilution rate. It can be seen that the measured values are more centrally distributed on both sides of the fitted straight line, which also suggests that the proposed model is highly accurate [10,26]. In summary, the insignificant factors in the model were removed to develop a quadratic regression model for the effect of process parameters on the dilution rate. The final regression model for the dilution rate is as follows:

$$\eta = 0.34 + 0.023A + 0.020B - 0.012C + 9.505 \times 10^{-3} \times B^2 \quad (10)$$

where A, B, and C in Equation (10) can be found in Table 5.

Table 5. ANOVA for the dilution rate.

	Sum of Square	Freedom Degrees	Mean Squares	*F*-Value	*p*-Value	
A Laser power	0.016	4	3.984×10^{-3}	25.68	<0.0001	Significant
B Scanning speed	7.100×10^{-3}	1	7.100×10^{-3}	45.77	<0.0001	
A^2	5.487×10^{-3}	1	5.487×10^{-3}	35.37	<0.0001	
B^2	2.023×10^{-3}	1	2.023×10^{-3}	13.04	0.0026	
C^2	1.326×10^{-3}	1	1.326×10^{-3}	8.55	0.0105	
Residual	2.327×10^{-3}	15	1.551×10^{-4}			
Anomaly	1.659×10^{-3}	10	1.659×10^{-4}	1.24	0.4289	Not significant
Pure error	6.680×10^{-4}	5	1.336×10^{-4}			
Sum of all	0.018	19				
Standard deviation	0.012		R^2	0.8726		
Mean	0.34		Adjusted R^2	0.8386		
Variation coefficient	3.63		Projected R^2	0.7616		
Predicting the residual sum of squares	4.353×10^{-3}		Signal-to-noise ratio	17.668		

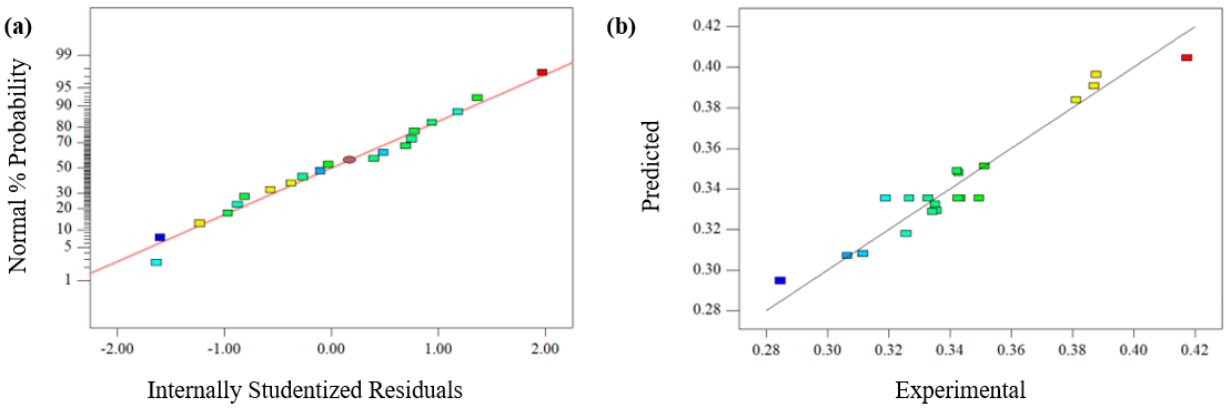

Figure 8. Fitting of process parameters to dilution ratio: (**a**) residual and (**b**) comparison of measured and predicted.

As can be seen from Table 5, the *p*-values of laser power, scanning speed, and powder feed rate are all less than 0.05, and the *p*-values of the first two parameters are less than 0.0001, indicating that the effects of these two parameters are most significant. Figure 9a shows the response of laser power and scanning speed to the dilution rate. As the laser power and scanning speed decrease, the dilution rate gradually decreases. During the DED process, the diminished laser power would reduce the melting of the substrate and decrease the depth of the melt pool [8,27]. Decreasing the scanning speed can increase the amount of molten pool powder injected per unit of time, increasing the deposition height and thus reducing the dilution rate [28]. Therefore, a smaller dilution rate can be obtained by increasing the powder feed rate and decreasing the laser power, as shown in Figure 9b.

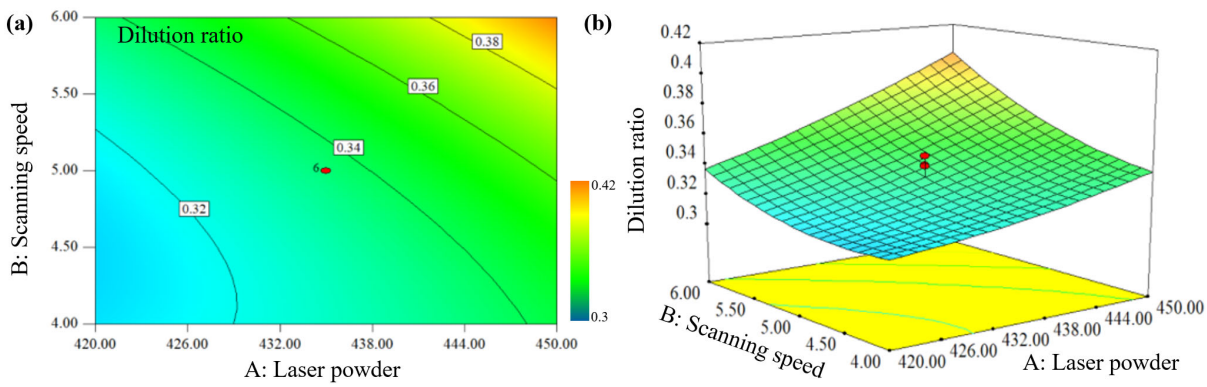

Figure 9. Response of laser power and scanning speed to dilution ratio: (**a**) contour plot, (**b**) 3D surface.

4.3. Response Surface Analysis for Microhardness

The ANOVA results for the effect of process parameters on microhardness are shown in Table 6. It can be seen that the *F*-value is 45.15 with a *p*-value of less than 0.0001, indicating that the established quadratic regression model for microhardness is valid and highly significant. Its misfit is not substantial, proving that the fitted equation is reliable. The signal-to-noise ratio of 22.800 is more than 4, indicating a high degree of precision and accuracy. The R^2 value of 0.9542 indicates a robust correlation. The residual plots of the microhardness model are shown in Figure 10a. No anomalous values are found in the plot, which suggests that the model has a high degree of confidence. Figure 10b plots the measured microhardness values against the predicted values [29,30]. It can be seen that the measured values are more centrally distributed on both sides of the fitted straight line, which also indicates the high accuracy of the regression model [31]. In summary, the

insignificant factors in the model were removed to construct a quadratic regression model for the effect of process parameters on microhardness. The fitting equation is shown below:

$$HV_{0.3} = 457.13 - 7.18A + 12.40B + 3.17C - 11.84A^2 - 2.76B^2 - 4.13C^2 \quad (11)$$

where A, B, and C in Equation (11) can be found in Table 6.

Table 6. ANOVA for the microhardness.

	Sum of Square	Freedom Degrees	Mean Squares	*F*-Value	*p*-Value	
Model	5113.74	6	852.29	45.15	<0.0001	Significant
A Laser power	704.91	1	704.91	37.34	<0.0001	
B Sanning speed	2099.71	1	2099.71	111.23	<0.0001	
C Powder feed rate	137.28	1	137.28	7.27	0.0183	
A^2	2019.38	1	2019.38	106.97	<0.0001	
B^2	109.92	1	109.92	5.82	0.0313	
C^2	245.60	1	245.60	13.01	0.0032	
Residual	245.41	13	18.88			
Anomaly	72.47	8	9.06	0.26	0.9541	Not significant
Pure error	172.94	5	34.59			
Sum of all	5359.15	19				
Standard deviation	4.34		R^2	0.9542		
Mean	444.34		Adjusted R^2	0.9331		
Variation coefficient	0.98		Projected R^2	0.9097		
Predicting the residual sum of squares	484.01		Signal-to-noise ratio	22.800		

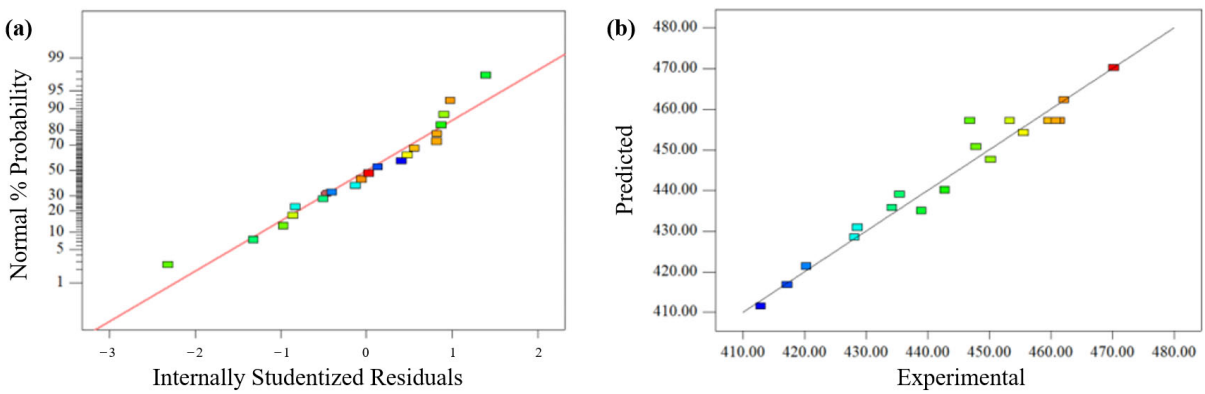

Figure 10. Fitting of process parameters to microhardness: (**a**) residual and (**b**) comparison of measured and predicted.

It can be seen from Table 6 that the *p*-values of laser power, scanning speed, and powder feed rate are less than 0.05, indicating that the effect of these three parameters on microhardness is significant. The scanning speed has the largest *F*-value, suggesting that it is the most significant essential factor. Figure 11a shows the contour plots and 3D response surfaces of the effects of process parameters on microhardness. The microhardness of the single tracks decreases as the laser power increases. However, the microhardness gradually increases with increasing scanning speed. On the one hand, as the laser power increases, the single-track height gradually increases, and the dilution rate decreases. On the other hand, as the scanning speed increases, the dilution rate gradually decreases. Because the microhardness of the deposited material is significantly higher than that of the substrate, the dilution of the molten pool by the substrate material decreases, and the microhardness of the single tracks increases significantly, as shown in Figure 11b.

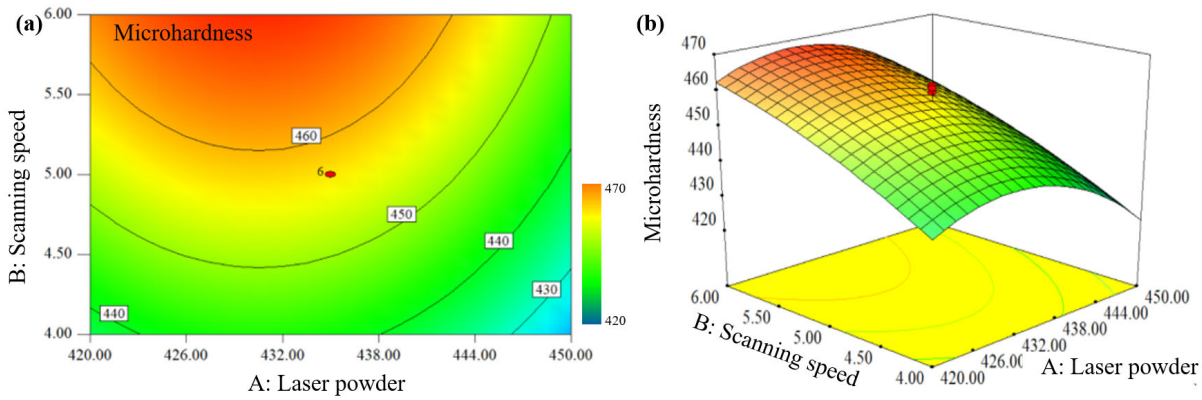

Figure 11. Response of laser power and scanning speed to microhardness: (**a**) contour plot, (**b**) 3D surface.

4.4. Multi-Response Optimization of Process Parameters

Based on the multi-objective optimization theory, this study aimed to obtain the maximum aspect ratio, the maximum microhardness, and the minimum dilution rate. A range of process parameter levels was set as the constraints, and the multi-objective optimization of laser cladding process parameters was realized with the help of the Design Expert software. The settings and weights for each process parameter and response target are shown in Table 7. The optimal combination of process parameters for laser cladding Ni-based powder on U71Mn rails obtained by the response surface method is a laser power of 431 W, a scanning speed of 5.34 mm/s, and a powder feed rate of 1.03 r/min. Based on the combination of the above process parameters, a single-pass cladding experiment was carried out. The measurements of each index were repeated three times to obtain the average value, and the results are shown in Table 8. The error between the theoretical prediction and the measured value is not more than 10%, and the experimental results align with the expected requirements. The above analysis demonstrates the high accuracy of the response surface model in predicting the experimental results and further illustrates the reliability of this model.

Table 7. Optimization criteria and targets.

Constraints					
Items	**Target**	**Lower Limit**	**Upper Limit**	**Weights**	**Significant**
A: Laser power	Inside the range	409.77	460.23	1	3
B: Scanning speed	Inside the range	3.32	6.68	1	3
C: Powder feed rate	Within range	0.83	1.17	1	3
Aspect ratio	Maximum value	2.01	3.22	1	3
Dilution ratio	Minimum value	0.2845	0.4174	1	3
Microhardness	Maximum value	412.81	470.26	1	3

Table 8. Comparison between predicted optimization and experimental validation.

	Predicted	**Experimental**	**Optimized Sectional Morphology**
Laser power (W)	431	431	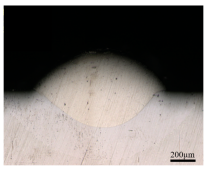
Powder feed (r/min)	5.34	5.34	
Scanning speed (mm/s)	1.03	1.03	
Aspect ratio	2.93	3.12	
Dilution ratio	0.330	0.354	
Microhardness ($HV_{0.3}$)	462.9	470.8	

4.5. Clad Microstructure Analysis

The temperature field distribution during the laser DED process affects the solidification behavior of the molten pool, where the temperature gradient (*G*) and the solidification

rate (R) are the key parameters that determine solidified grain morphology [32,33]. We have previously developed a finite element model [24] that mainly includes heat and mass transfer, material properties, solution region, and boundary condition settings to simulate the laser cladding process for Ni-based powder on U71Mn rail steel. The G and R can be represented as follows:

$$G = \nabla T \cdot \vec{n_s} \tag{12}$$

$$R = V_s \cos\theta \tag{13}$$

where θ denotes the angle between the normal to the solidification front and the scanning speed, as shown in Figure 12. As solidification proceeds, the θ decreases, indicating a gradual increase in the R from the bottom to the top of the melt pool.

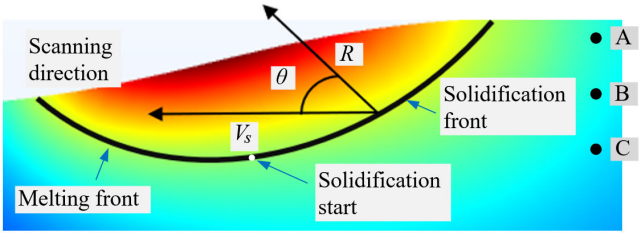

Figure 12. Schematic diagram of solidification rate versus scanning speed.

According to the theory of rapid solidification, the morphology and size of the grains in the cladding layer are subject to the combined effect of G and R [34]. The detailed pattern is shown in Figure 13. It can be seen from Figure 13 that as G/R decreases, the microstructure morphology transforms from planar grains to cellular, columnar, and equiaxial grains. Moreover, the size of the microstructure decreases gradually with an increase in R.

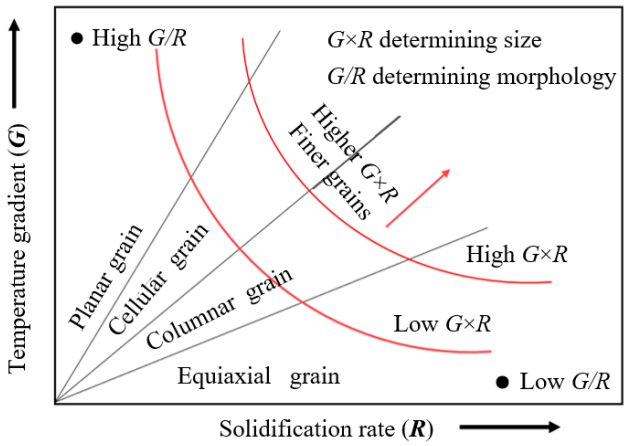

Figure 13. Temperature gradient vs. solidification rate plot defining the grain morphology during solidification [35,36].

The curves of temperature variation with time at three points A, B, and C at the top, middle, and bottom locations of the cross section (Figure 12) were obtained, and the results are shown in Figure 14. It can be seen in Figure 14 that the maximum cooling rates at points A and C during solidification are 3080 and 795 K/s, respectively. Because the surface of the melt pool is closer to the laser heat source than other locations, the G gradually increases from the top to the bottom, and the R of the cladding layer gradually decreases from the surface to the bottom [37].

The grain morphologies at different locations (points A, B, and C) of the optimized single-track, shown in Figure 15. At the top position of the cladding (point A), because G/S is low and $G \times S$ is high, the microstructure in this region exists mainly in the form of refined equiaxed grains. At the middle position of the cladding (point B), the microstructure

primarily exists in the form of equiaxial grains and some columnar grains. However, the full planar grains as well as cellular grains are observed at the bottom position of the cladding layer (point C). This experimental result verifies the above simulation predictions. In addition, it can also be seen that a good metallurgical bond is formed between the cladding layer and the substrate [38].

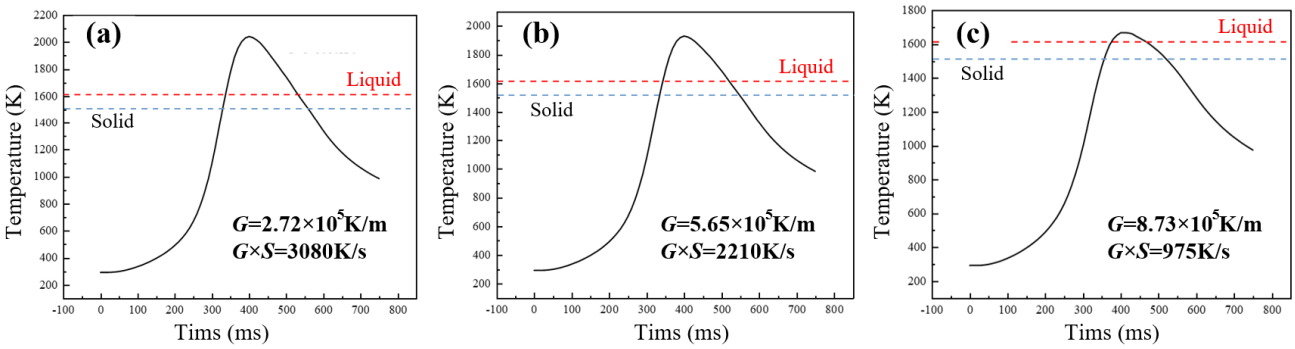

Figure 14. Curve of temperature variation with time: (**a**) point A, (**b**) point B, and (**c**) point C.

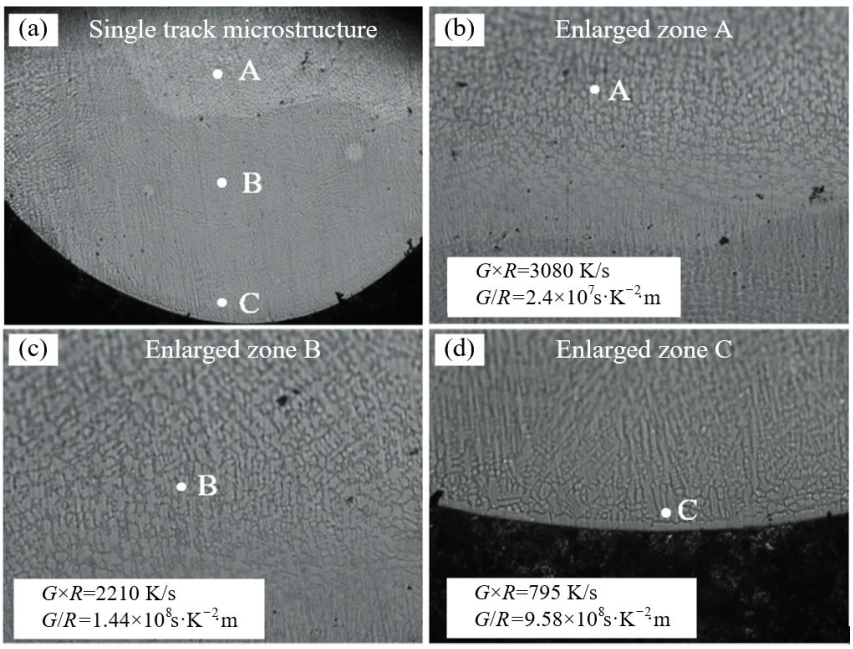

Figure 15. The positions of points A, B, and C in the cladding layer and their corresponding grains.

5. Conclusions

This study developed a quadratic regression model on the relationship between response targets (aspect ratio, dilution rate, and microhardness) and process parameters with the help of ANOVA. The response surface was employed to optimize the process parameters and a suitable combination of process parameters for laser DED deposition of Ni-based alloys on U71Mn steel. The multi-objective optimization of the geometrical morphology and microhardness of the single tracks was realized. The main conclusions are as follows:

1. ANOVA and 3D response surface plots indicate that scanning speed has the most significant effect on aspect ratio. At the same time, the dilution ratio and microhardness are mainly driven by the laser power and scanning speed.
2. The response objectives (aspect ratio, dilution rate, and microhardness) were transformed into single goals to be optimized by response surface design. The optimized

combination of process parameters to satisfy the response objectives was obtained and experimentally verified.

3. The error between the predicted and experimental response targets is not more than 10%, which also indicates the validity and reliability of the model. The optimal combination of process parameters is a laser power of 431 W, a scanning speed of 5.34 mm/s, and a powder feed rate of 1.03 r/min. The microhardness of the clad fabricated by these process parameters is 470.8 HV.
4. During the solidification of the single track, the cooling rate gradually increases from 795 to 3080 K/s from the bottom to the top, while the solidification rate gradually increases from 0.0039 to 0.011 m/s. As a result, the microstructure morphology transforms from planar grains to a mixture of cellular and columellar grains, and the size of the grains decreases.

Author Contributions: Methodology, J.L., T.Y., J.Z. and Z.W.; Software, L.C.; Validation, Y.Y. and L.C.; Investigation, Z.W.; Resources, Y.Y.; Writing—original draft, J.L.; Writing—review & editing, J.L.; Supervision, T.Y.; Project administration, T.Y. and J.Z.; Funding acquisition, J.Z. All authors have read and agreed to the published version of the manuscript.

Funding: This work is supported by the National Natural Science Foundation of China (52075088) and 111Project (B16009).

Institutional Review Board Statement: Not applicable.

Informed Consent Statement: Not applicable.

Data Availability Statement: Data are contained within the article.

Conflicts of Interest: We declare that we have no financial or personal relationships with other people or organizations that can inappropriately influence our work. There is no professional or other personal interest of any nature or kind in any product, service, or company that could be construed as influencing the position presented in, or the review of, the manuscript entitled "Multi-Objective Optimization of Process Parameters in Laser DED Ni-Based Powder on Steel Rail Using Response Surface Design".

References

1. Clare, A.; Oyelola, O.; Folkes, J.; Farayibi, P. Laser cladding for railway repair and preventative maintenance. *J. Laser Appl.* **2012**, *24*, 32004. [CrossRef]
2. Ding, H.; Yang, T.; Wang, W.; Zhu, Y.; Lin, Q.; Guo, J.; Xiao, Q.; Gan, L.; Liu, Q. Optimization and wear behaviors of 316L stainless steel laser cladding on rail material. *Wear* **2023**, *523*, 204830. [CrossRef]
3. Pointner, P. High strength rail steels—The importance of material properties in contact mechanics problems. *Wear* **2008**, *265*, 1373–1379. [CrossRef]
4. Lai, Q.; Abrahams, R.; Yan, W.; Qiu, C.; Mutton, P.; Paradowska, A.; Soodi, M. Investigation of a novel functionally graded material for the repair of premium hypereutectoid rails using laser cladding technology. *Compos. Part B Eng.* **2017**, *130*, 174–191. [CrossRef]
5. DebRoy, T.; Wei, H.L.; Zuback, J.S.; Mukherjee, T.; Elmer, J.W.; Milewski, J.O.; Beese, A.M.; Wilson-Heid, A.; De, A.; Zhang, W. Additive manufacturing of metallic components–Process, structure and properties. *Prog. Mater. Sci.* **2018**, *92*, 112–224. [CrossRef]
6. Svetlizky, D.; Das, M.; Zheng, B.; Vyatskikh, A.L.; Bose, S.; Bandyopadhyay, A.; Schoenung, J.M.; Lavernia, E.J.; Eliaz, N. Directed energy deposition (DED) additive manufacturing: Physical characteristics, defects, challenges and applications. *Mater. Today* **2021**, *49*, 271–295. [CrossRef]
7. Chen, L.; Zhao, Y.; Chen, X.; Yu, T.; Xu, P. Repair of spline shaft by laser-cladding coarse TiC reinforced Ni-based coating: Process, microstructure and properties. *Ceram. Int.* **2021**, *47*, 30113–30128. [CrossRef]
8. Chen, L.; Yu, T.; Xu, P.; Zhang, B. In-situ NbC reinforced Fe-based coating by laser cladding: Simulation and experiment. *Surf. Coat. Technol.* **2021**, *412*, 127027. [CrossRef]
9. Morville, S.; Carin, M.; Peyre, P.; Gharbi, M.; Carron, D.; Le Masson, P.; Fabbro, R. 2D longitudinal modeling of heat transfer and fluid flow during multilayered direct laser metal deposition process. *J. Laser Appl.* **2012**, *24*, 032008. [CrossRef]
10. Singh, A.K.; Sadhu, A.; Das, A.K.; Pratihar, D.K.; Choudhury, A.R. An approach towards energy and material efficient additive manufacturing: Multi-objective optimization of stellite-6 deposition on SS304. *Opt. Laser Technol.* **2021**, *148*, 107799. [CrossRef]
11. Ma, M.; Xiong, W.; Lian, Y.; Han, D.; Zhao, C.; Zhang, J. Modeling and optimization for laser cladding via multi-objective quantum-behaved particle swarm optimization algorithm. *Surf. Coat. Technol.* **2019**, *381*, 125129. [CrossRef]

12. Ansari, M.; Razavi, R.S.; Barekat, M. An empirical-statistical model for coaxial laser cladding of NiCrAlY powder on Inconel 738 superalloy. *Opt. Laser Technol.* **2016**, *86*, 136–144. [CrossRef]
13. Alimardani, M.; Toyserkani, E. Prediction of laser solid freeform fabrication using neuro-fuzzy method. *Appl. Soft Comput.* **2008**, *8*, 316–323. [CrossRef]
14. Chen, L.; Bi, G.; Yao, X.; Tan, C.; Su, J.; Ng, N.P.H.; Chew, Y.; Liu, K.; Moon, S.K. Multisensor fusion-based digital twin for localized quality prediction in robotic laser-directed energy deposition. *Robot. Comput. Manuf.* **2023**, *84*, 102581. [CrossRef]
15. Sohrabpoor, H. Analysis of laser powder deposition parameters: ANFIS modeling and ICA optimization. *Optik* **2016**, *127*, 4031–4038. [CrossRef]
16. Guo, S.; Chen, Z.; Cai, D.; Zhang, Q.; Kovalenko, V.; Yao, J. Prediction of Simulating and Experiments for Co-based Alloy Laser Cladding by HPDL. *Phys. Procedia* **2013**, *50*, 375–382. [CrossRef]
17. Wu, Z.; Li, T.; Li, Q.; Shi, B.; Li, X.; Wang, X.; Lu, H.; Zhang, H.-C. Process optimization of laser cladding Ni60A alloy coating in remanufacturing. *Opt. Laser Technol.* **2019**, *120*, 105718. [CrossRef]
18. Javid, Y. Multi-response optimization in laser cladding process of WC powder on Inconel 718. *CIRP J. Manuf. Sci. Technol.* **2020**, *31*, 406–417. [CrossRef]
19. Meng, G.; Zhu, L.; Zhang, J.; Yang, Z.; Xue, P. Statistical analysis and multi-objective process optimization of laser cladding TiC-Inconel718 composite coating. *Optik* **2021**, *240*, 166828. [CrossRef]
20. Grohol, C.M.; Shin, Y.C.; Frank, A. Laser cladding of aluminum alloy 6061 via off-axis powder injection. *Surf. Coat. Technol.* **2021**, *415*, 127099. [CrossRef]
21. Olakanmi, E.; Nyadongo, S.; Malikongwa, K.; Lawal, S.; Botes, A.; Pityana, S. Multi-variable optimisation of the quality characteristics of fiber-laser cladded Inconel-625 composite coatings. *Surf. Coatings Technol.* **2018**, *357*, 289–303. [CrossRef]
22. Chen, L.; Yu, T.; Chen, X.; Zhao, Y.; Guan, C. Process optimization, microstructure and microhardness of coaxial laser cladding TiC reinforced Ni-based composite coatings. *Opt. Laser Technol.* **2022**, *152*, 108129. [CrossRef]
23. Li, Q.; Chen, J.; Wang, X.; Liu, Y.; Jiang, K.; Yang, S.; Liu, Y. Process, microstructure and microhardness of GH3039 superalloy processed by laser metal wire deposition. *J. Alloys Compd.* **2021**, *877*, 160330. [CrossRef]
24. Chen, L.; Zhao, Y.; Song, B.; Yu, T.; Liu, Z. Modeling and simulation of 3D geometry prediction and dynamic solidification behavior of Fe-based coatings by laser cladding. *Opt. Laser Technol.* **2021**, *139*, 107009. [CrossRef]
25. Li, C.; Yu, Z.; Gao, J.; Zhao, J.; Han, X. Numerical simulation and experimental study of cladding Fe60 on an ASTM 1045 substrate by laser cladding. *Surf. Coat. Technol.* **2018**, *357*, 965–977. [CrossRef]
26. Mondal, S.; Paul, C.P.; Kukreja, L.M.; Bandyopadhyay, A.; Pal, P.K. Application of Taguchi-based gray relational analysis for evaluating the optimal laser cladding parameters for AISI1040 steel plane surface. *Int. J. Adv. Manuf. Technol.* **2012**, *66*, 91–96. [CrossRef]
27. Han, B.; Li, R.; Pi, Q.; Shi, Y.; Qi, H.; Bi, K.; Sun, G. Prediction of deposit characteristics based on the discrete coaxial nozzle during laser direct metal deposition. *Opt. Laser Technol.* **2023**, *163*, 109385. [CrossRef]
28. Wirth, F.; Wegener, K. A physical modeling and predictive simulation of the laser cladding process. *Addit. Manuf.* **2018**, *22*, 307–319. [CrossRef]
29. Sun, Y.; Hao, M. Statistical analysis and optimization of process parameters in Ti6Al4V laser cladding using Nd:YAG laser. *Opt. Lasers Eng.* **2012**, *50*, 985–995. [CrossRef]
30. Farayibi, P.K.; Abioye, T.E.; Clare, A.T. A parametric study on laser cladding of Ti-6Al-4V wire and WC/W2C powder. *Int. J. Adv. Manuf. Technol.* **2016**, *87*, 3349–3358. [CrossRef]
31. Costa, L.; Felde, I.; Réti, T.; Kálazi, Z.; Colaço, R.; Vilar, R.; Verő, B. A Simplified Semi-Empirical Method to Select the Processing Parameters for Laser Clad Coatings. *Mater. Sci. Forum* **2003**, *414–415*, 385–394. [CrossRef]
32. Liu, H.; Li, M.; Qin, X.; Huang, S.; Hong, F. Numerical simulation and experimental analysis of wide-beam laser cladding. *Int. J. Adv. Manuf. Technol.* **2018**, *100*, 237–249. [CrossRef]
33. Jin, K.; Yang, Z.; Chen, P.; Huang, G.; Qiao, X. Dynamic solidification process during laser cladding of IN718: Multi-physics model, solute suppressed nucleation and microstructure evolution. *Int. J. Heat Mass Transf.* **2022**, *192*, 122907. [CrossRef]
34. Wang, H.-Z.; Cheng, Y.-H.; Zhang, X.-C.; Yang, J.-Y.; Cao, C.-M. Effect of laser scanning speed on microstructure and properties of Fe based amorphous/ nanocrystalline cladding coatings. *Mater. Chem. Phys.* **2020**, *250*, 123091. [CrossRef]
35. Chen, L.; Yu, T.; Chen, Y.; Wang, W. Slicing strategy and process of laser direct metal deposition (DMD) of the inclined thin-walled part under open-loop control. *Rapid Prototyp. J.* 2021, *ahead of print*. [CrossRef]
36. Muvvala, G.; Karmakar, D.P.; Nath, A.K. In-process detection of microstructural changes in laser cladding of in-situ Inconel 718/TiC metal matrix composite coating. *J. Alloys Compd.* **2018**, *740*, 545–558. [CrossRef]
37. Mishra, A.K.; Kumar, A. Numerical and experimental analysis of the effect of volumetric energy absorption in powder layer on thermal-fluidic transport in selective laser melting of Ti6Al4V. *Opt. Laser Technol.* **2018**, *111*, 227–239. [CrossRef]
38. Salloom, R.; Joshi, S.; Dahotre, N.; Srinivasan, S. Laser surface engineering of B4C/Fe nano composite coating on low carbon steel: Experimental coupled with computational approach. *Mater. Des.* **2020**, *190*, 108576. [CrossRef]